Received: 7 October 2022 | Accepted: 17 November 2022

DOI: 10.1002/pamm.202200193

Injection molding of semi-crystalline polymers in a space-time framework

Blanca Ferrer Fabón[1,*], **Jonathan Alms**[2], **Marek Behr**[1], and **Christian Hopmann**[2]

[1] Chair for Computational Analysis of Technical Systems (CATS), RWTH Aachen University, 52056 Aachen, Germany
[2] Institute of Plastics Processing (IKV), RWTH Aachen University, 52056 Aachen, Germany

The challenges in the numerical simulation of the polymer injection molding process are manifold. Such simulation involves a two-phase flow formulation and the physical modeling of complex material, i.e., molten polymer. This paper presents a complete macroscale simulation approach for the filling stage of injection molding with semi-crystalline polymers, applied on polypropylene as example. Accurate and efficient results are obtained using a space-time finite-element discretization. Heading towards more efficient computations, we search for a reduction of the polymer's physical model, which includes variable viscosity, density, and several crystallization models. The final contribution of the present work is a model sensitivity analysis, which evaluates the relevance of each material model during the filling stage of injection molding.

1 Introduction

Nowadays, most industrial processes are modeled, studied, and controlled with computer assistance. This allows not only to optimize the process, but also to improve the final product, and to fulfill the demanding accuracy requirements of today's industry. In the case of the widely used process of polymer injection molding, the prevention of manufacturing defects, such as warpage, residual stresses, air entrapment, or shrinkage, is a core factor in avoiding failure or malfunction of the final molded component. The high-resolution computational analysis plays a major role here. However, the challenges of the simulation of molding process are manifold, and high-resolution and efficient numerical methods in this field are still being developed and analyzed.

In this study, we consider the computational model of the polymer during the injection phase. We use an in-house finite-elements solver XNS to simulate the polymer and air flow in the cavity as a two-phase flow. To distinguish between the air and the polymer phase, we use the level-set approach [1], which captures the interface of the two-phase flow. For the polymer characterization, we apply the non-Newtonian Cross-WLF rheology model [2], and for the solidification process, we implement a pvT model [3, 4]. To extend that model to semi-crystalline polymers, we use the Nakamura [5] and the Hoffman-Lauritzen models [6] to describe the crystallization process.

2 Governing equations and solution technique

The injection molding process is described as a two-phase flow governed by the transient incompressible Navier-Stokes equations coupled with the heat equation. Two additional transport equations are coupled to the main equations, corresponding to the polymer crystallization and the level-set method.

We consider a computational domain $\Omega \subset \mathbb{R}^2$ enclosing the immiscible time-varying subdomains representing the air $\Omega_1(t)$ and polymer phases $\Omega_2(t)$, where $\Omega_1(t) \cup \Omega_2(t) = \Omega$. The interface between these two phases is denoted as $\Gamma_{int}(t) = \Omega_1(t) \cap \Omega_2(t)$, while the boundary of the entire domain is defined as $\Gamma = \partial\Omega$.

At each instant $t \in [0, t_{final}]$, velocity $\mathbf{u}(x,t)$, pressure $p(x,t)$, and temperature $T(x,t)$ in each phase i in the subdomain $\Omega_i(t)$ are described by:

$$\rho_i \left(\frac{\partial \mathbf{u}}{\partial t} + \mathbf{u} \cdot \nabla \mathbf{u} - \mathbf{f} \right) - \nabla \cdot \boldsymbol{\sigma}_i = \mathbf{0}, \tag{1}$$

$$\nabla \cdot \mathbf{u} = 0, \tag{2}$$

$$\rho_i C_{p,i} \left(\frac{\partial T}{\partial t} + \mathbf{u} \cdot \nabla T \right) - k_i \nabla^2 T - \Phi_i - \Xi_i = 0, \tag{3}$$

where ρ corresponds to the density, $\mathbf{f}$ represents the body force, and $\boldsymbol{\sigma}$ is the stress tensor, including viscous and pressure contributions. In the heat equation, Eq. (3), C_p represents isobaric heat capacity, k thermal conductivity, Φ viscous heat dissipation, and Ξ crystallization heat source. Indices $i = 1, 2$ correspond to each of the material phases. Specifically, the stress tensor, the heat dissipation, and the crystallization heat source are:

$$\boldsymbol{\sigma}_i = -p\mathbf{I} + \mu_{eff,i} \left(\nabla \mathbf{u} + (\nabla \mathbf{u})^T \right), \tag{4}$$

* Corresponding author: e-mail ferrer@cats.rwth-aachen.de, phone +49 241 80 99931, fax +49 241 80 99910

$$\Phi_i = \mu_{eff,i} \left(\nabla \mathbf{u} + (\nabla \mathbf{u})^T\right) : \left(\nabla \mathbf{u} + (\nabla \mathbf{u})^T\right), \tag{5}$$

$$\Xi_i = \rho_i \xi_{max,i}^{abs} \Delta H_{c,i} \frac{\partial \xi}{\partial t}, \tag{6}$$

where μ_{eff} represents the effective dynamic viscosity, defined in Eq. (9). In the crystallization heat source definition, ξ_{max}^{abs} is the absolute maximum degree of crystallization and ΔH_c is the latent heat of crystallization, both characteristic values of the considered polymer. The ξ represents the relative degree of crystallization, which is defined as $\xi = \frac{\xi_{abs}}{\xi_{max}^{abs}}$.

The constant material properties in Eqs. (1)–(6) for both the polymer and the air phase are in Tables 1 and 2, respectively.

Table 1: Material constants for PP505P.

Constant	Value	Constant	Value
k	0.22 W/mK	T_∞	231.15 K
$C_{p,crystal}$	2000 J/(kg K)	$T_{m,0}$	467.15 K
$C_{p,amorphous}$	2667 J/(kg K)	R	8.31446 J/(K mol)
ξ_{max}^{abs}	0.49	U^*	17200 J/mol
ΔH_c	$1.90 \cdot 10^5$ J/kg		

Table 2: Material constants for air.

Constant	Value
ρ	0.8 kg/m^3
μ	$2 \cdot 10^{-5}$ kg/(m s)
k	0.025 W/(m K)
C_p	1000 J/(kg K)

To capture the interface between phases, we use the level-set method. The signed function ϕ is transported with the flow velocity $\mathbf{u}$:

$$\frac{\partial \phi}{\partial t} + \mathbf{u} \cdot \nabla \phi = 0. \tag{7}$$

In order to discretize Eqs. (1)–(3) and (7), we use P1P1 finite elements with the Galerkin/Least-Squares (GLS) stabilization [7]. For higher computational efficiency, we use space-time discretization [8]. This method allows adapting time resolution locally in the areas of interest, including the vicinity of the moving interface [9]. However, in this preliminary work, we still use discontinuous prismatic space-time (D-PST) basis, i.e., with no refinement in time.

3 Material models

An isotactic polypropylene (i-PP) PP505P from Sabic is used to demonstrate new simulation approaches to increase the accuracy of predicting shrinkage and warpage of an injection molded part. The pvT behavior and the model for viscosity are adopted from literature [2–4].

The pvT behavior is modeled by a two-domain Tait model, where the specific volume v is dependent on temperature T and pressure p. In this model, a transition temperature distinguishes between solid and liquid domains, with their corresponding specific volume ν formulations. The specific formulation of the Tait model is given in [3, 4] and the used model parameters in [11].

$$v = \rho^{-1} = f(T, p) \tag{8}$$

The viscosity model assumes the polymer melt as a non-Newtonian fluid considering shear ($\dot{\gamma}$) thinning and a pressure and temperature dependency of the zero viscosity μ_0 in a Cross-WLF model [2]. The specific formulation and model parameters are given in [11]. We do not consider any crystallization correction for this model.

$$\mu_{eff} = \mu_{amorphous} = f(\mu_0(T, p), \dot{\gamma}) \tag{9}$$

4 Crystallization approach

The model of the crystallization ξ applied in the simulation uses the Nakamura expression of the Avrami equation (10) where the crystallization rate constant K_a is expressed as a function of temperature T and n_a is the Avrami-coefficient, which characterizes the spherulitic growth mechanisms.

$$\xi = 1 - exp(-(K_a(T)t)^{n_a}) \tag{10}$$

An Avrami coefficient of around 3 was measured in previous studies and is fixed to 3 here [13]. This assumes heterogeneous nucleation either from thermal processes or on contaminations and a three-dimensional spherulitic growth [14–16]. The crystallization rate constant is explained by the Hoffman-Lauritzen equation using the half-crystallization time $(1/t_{1/2})_0$ extension replacing the growth function from the original Hoffman-Lauritzen equation (11) [17, 18]. Replacing the growth

function by the constant half-crystallisation time allows a reduction of complexity. Therefore, computational efficiency increases, since only relative crystallization is calculated on a macro-scale, but not the growth of local forming spherulites on a micro-scale level.

$$K_a(T) = ln(2)^{1/n_a} \cdot \left(\frac{1}{t_{1/2}}\right)_0 \cdot exp\left(-\frac{U^*}{R(T-T_\infty)}\right) \cdot exp\left(-\frac{K_g(T_{m,0}+T)}{2T^2(T_{m,0}-T)}\right) \tag{11}$$

Here, K_g is a material parameter; U^* is the activation energy for the segmental jump rate in polymers; $T_\infty = T_g - 50$ K with T_g being the glass transition temperature; $T_{m,0}$ is the equilibrium melting temperature and R being the universal gas constant [17, 19] (see Table 1).

The evaluation of K_g and $(1/t_{1/2})_0$ is performed by fitting the relative crystallization to measurements performed by DSC and Flash-DSC for 8 different cooling rates $\dot{T}$ using Eq. (12):

$$\ln\left(\frac{(-ln(1-\xi))^{\frac{1}{n_a}}}{ln(2)^{\frac{1}{n_a}}}\right) = \ln\left(\frac{1}{t_{\frac{1}{2}}}\right)_0 - \frac{U^*}{R\,(T-T_\infty)} - \frac{K_g\,(T_{m,0}+T)}{2T^2\,(T_{m,0}-T)} + \ln\left(\frac{T_{start}-T}{\dot{T}}\right). \tag{12}$$

The time t resulting from the Avrami equation (10) is replaced by the difference between the onset crystallization temperature T_{start} and the current temperature divided by the fixed cooling rate which is applied in the DSC or Flash-DSC measurements. For 8 cooling rates, the fitted parameters for the half-crystallization time and for the material constant K_g are shown in Table 3, where R^2 is the coefficient of determination. The fit indicates a good agreement with the data, except for the 100 K/s cooling rate. However, this is to be expected, since at 50 and 100 K/s cooling rate, a second crystallization phase forms, which does not show spherulitic growth and is neglected here. We recognize that in real melts multiple cooling rates occur throughout the whole component. For simplification purposes we fixed the half-crystallization time and Kg to the values in Table 4. This fixes the crystallization function to be independent of local cooling rate, but we use the simplification to show that our approach is able to consider cooling-rate-dependent crystallization.

Table 3: Eq. (12) fitting results for the material constant K_g and the half crystallization time.

Measurement device	**DSC**					**Flash-DSC**		
Cooling rate [K/s]	0.033	0.083	0.166	0.207	0.333	10	50	100
$ln(1/t_{1/2})_0$	49.75	27.96	29.55	25.71	28.20	33.60	51.15	61.82
$K_g \cdot 10^{-6}$	1.385	0.533	0.568	0.447	0.515	0.580	1.146	1.496
R^2	0.932	0.999	0.994	0.997	0.990	0.992	0.903	0.608

Table 4: Fitted parameters.

Parameter	**Value**
K_g	$6.10 \cdot 10^{-6}$
$ln(1/t_{1/2})_0$	30
C_1	10
C_2	5500

In injection molding processes, the shear stresses are significant and they can affect the crystallization degree. With the purpose of simulating the crystallization due to shear stresses, we implement the model proposed by Guo and Narh [20]. This model adjusts the equilibrium melting temperature $T_{m,0}$ with the shear stresses as follows:

$$T_{m,0,corrected} = T_{m,0} + C_1 e^{-\frac{C_2}{\tau}}, \tag{13}$$

being C_1 and C_1 model fitting parameters. Its values are noted in Table 4.

One last material model adjustment due to crystallization is considered. The specific heat C_p depends on the crystallization degree. With the rule of mixture description in Eq. (14), we update the specific heat considering its values for the crystallized polymer $C_{p,crystal}$ and for the non-crystallized one $C_{p,amorphous}$. These are reported in Table 1.

$$C_p = C_{p,crystal} \cdot \xi \cdot \xi_{max}^{abs} + C_{p,amorphous} \cdot (1 - \xi \cdot \xi_{max}^{abs}) \tag{14}$$

5 Results

The geometry used in our tests is a 2-dimensional rectangular cavity of size 40×4 mm with an extra inlet cavity of 1×1 mm, see Fig. 1. At the initial condition, the air phase Ω_1 fills the main cavity and half of the inlet cavity, while the polymer subdomain Ω_2 is at the entry of the inlet cavity. A polymer velocity is imposed at the inlet, $v_{x,in} = 0.35$ m/s, while a free velocity boundary is prescribed at the outlet, where the pressure is set to 0 Pa. The wall boundary condition is varying in time and divided in three regions: $\Gamma_{wall} = \Gamma_{wall,polymer} + \Gamma_{wall,interface} + \Gamma_{wall,air}$. In the polymer phase, we apply a no-slip condition, while in the air phase, we apply a full slip condition. To avoid instabilities and convergence issues, we define a region in the vicinity of the phase interface Γ_{int}, where the wall boundary condition is a variable Navier slip, ramping up from slip to no-slip condition. The interface width is determined from the level-set field as $|\phi| < 5 \cdot 10^{-4}$.

The initial temperature field is 493.15 K in the inlet and 313.15 K in the rest of the domain. At the inlet, the temperature remains 493.15 K, and at the walls and outlet, we prescribe a Neumann boundary condition representing the cooling steel

plates with a heat transfer coefficient of 1666.67 W/K and an ambient temperature of 313.15 K. Crystallization is initially 0 and it is initiated at the inlet as $\xi_0 = 1 \cdot 10^{-12}$.

When using a fine unstructured triangular space-time mesh, Fig. 2**a**, with high refinement near the walls, the simulation becomes computationally expensive and encounters convergence issues. When simplifying the model, considering constant temperature and neglecting any crystallization effects, the compute time and convergence problems are highly diminished. In both simulations, as a result of the level-set and the Navier-slip condition properties, slight pressure jumps and mesh-dependent solutions near the phase interface Γ_{int} appear. In this work, we do not approach this problem directly, but we use a very-fine mesh ($h \sim 5 \cdot 10^{-2}$ mm) and small time-steps ($dt = 0.5$ ms) to avoid instabilities. A local time refinement only in the vicinity of the phase interface as in [21] would be advantageous in terms of computation efficiency. Figure 3 shows the level-set solution of the full and of the simplest model (constant temperature and no crystallization). We can observe how the solutions differ, especially in the early stage the filling; see Fig. 3**a**. At a later stage, in Fig. 3**b**, after the flow develops, the main differences remain near the wall.

Fig. 1: Injection molding cavity: Test geometry.

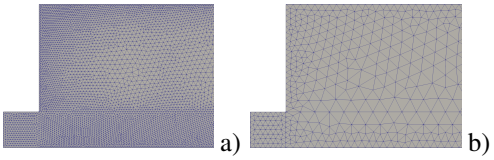

a) b)

Fig. 2: Section of the fine (**a**) and coarse (**b**) unstructured mesh.

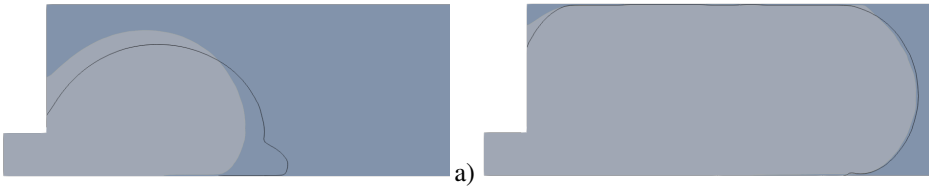

a) b)

Fig. 3 Level-set solution for the full model (background colors) and for the simple model (black line) at time steps 30 (**a**) and 90 (**b**).

6 Model sensitivity

In this section, we focus on simplifying the material model for the filling phase of the injection molding process. Since the results between the full and the simplest model differ strongly, we present a more specific comparison, exploring the effect of each material model individually. With the full model solution as a reference, and using a coarse mesh, see Fig. 2**b**, the simulation has been repeated. Maintaining all parameters fixed but deactivating one of the models at a time, we obtain 7 different simulations, one per deactivated model. The results obtained for each case are then compared with the reference solution, allowing us to determine the relevance of each model and therefore neglecting the non-relevant models.

In Fig. 4**a**, the reference simulation is shown, together with the flow front lines of the other models tested. What stands out in this figure is that the simulations with constant temperature and constant viscosity are the ones that depart the most, already in the early time steps, from the reference solution. The rest of the models are barely distinguishable since they qualitatively follow the reference solution.

Analyzing the solution at later time steps and zooming in on the Fig. 4**b**, we can see that some remaining models do slightly differ from the reference solution. To the extent of quantifying this change and its relevance, we present a quantitative analysis. First, the models affecting the temperature field (viscous dissipation, variable specific heat due crystallization, and crystallization heat source) are considered, comparing the temperature field of each simulation to the reference solution. For every time step, the relative error at each mesh node is computed and used to calculate the mean and maximum error values. In Fig. 5 these results are shown. The same procedure follows for the level-set field. In this case, we compute nodal absolute errors, and the mean and maximum values are calculated only with the nodes in the vicinity of the flow interface Γ_{int} instead of in the entire domain; see Fig. 6.

For the temperature field comparison in Fig. 5, we observe that the mean errors are minor, even though the maximum error can reach high values. Both graphics indicate that the viscous heat has more influence on the temperature solution than the rest of the models. However, the other two models, which depend directly on the crystallization field, clearly show error growth in time. This fact is understandable due to the crystallization's nature, which increases not just with temperature but with time. We observe this tendency in the level-set field comparison, Fig. 6: the effect of crystallization and crystallization due to shear becomes more relevant with time. Even though the mean absolute errors are negligible, the growing tendency indicates that the models will become relevant in the following time steps. In the last time steps, the maximum absolute deviation is already above $3 \cdot 10^{-5}$, which indicates a relevant change in the level-set, as $1 \cdot 10^{-5}$ corresponds to approximately half of the size of the smallest element; see Fig. 7. Regarding the rest of the models, the mean and maximum absolute errors are not significant

and have a constant tendency. Therefore, the effects of these models, the density Tait model and the viscous heat, can be neglected for the simulation of the filling stage of the injection molding process.

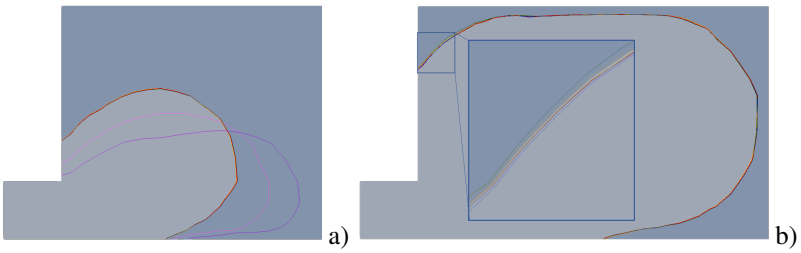

Fig. 4 Level-set solution for the complete model (background colors) and for deactivated models (lines): cross-WLF for viscosity (pink), constant temperature (purple), crystallization (green), crystallization due to shear stress (blue), crystallization heat (yellow), viscous heat (orange), rule of mixture for the specific heat (red), and Tait model for the density (black). Time-step 10 (**a**) and 50 (**b**).

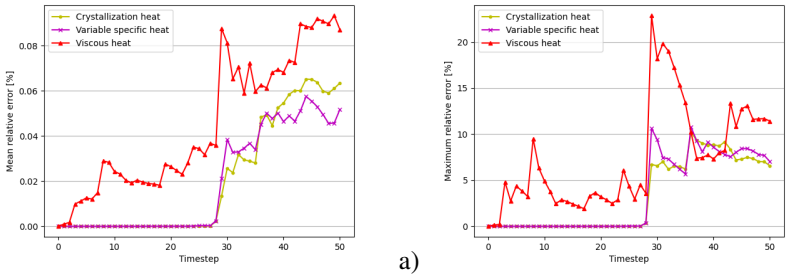

Fig. 5: Comparison of the temperature field solution between the complete model and the deactivated models. Mean (**a**) and maximum (**b**) relative errors.

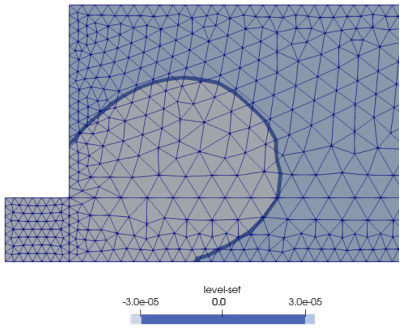

Fig. 7: Level-set solution example. Scale ranged from $3 \cdot 10^5$ to $3 \cdot 10^{-5}$.

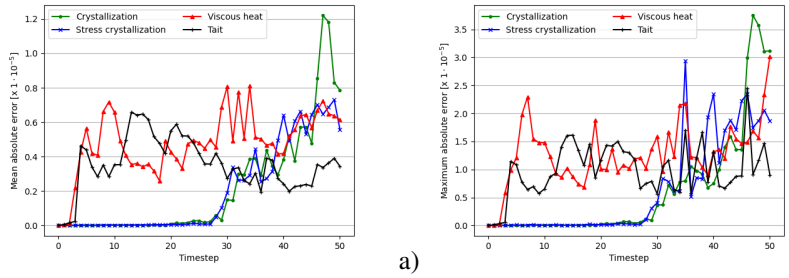

Fig. 6: Comparison of the level-set field solution between the complete model and the deactivated models. Mean (**a**) and maximum (**b**) absolute errors.

7 Outlook

From the sensitivity analysis of the considered models, we can conclude that the main models affecting the polymer flow behavior are the viscosity, dependent on temperature, pressure and shear stress, and the temperature field. Therefore, our efforts should focus on using accurate models for these quantities. At the same time, the density model and the viscous heat dissipation are not very relevant for these simulations. For all models depending on crystallization, we can state that they are not significant for the first simulation steps. Nonetheless, they become relevant with time, and we should already consider them for injection times higher than 50 ms. These conclusions apply only for the cavity filling simulation, i.e., for later stages of the injection molding process, such as dwelling and cooling, all models should be considered again.

With the reduced physical model, the main difficulty encountered in the simulation is the level-set and wall boundary condition, which requires a very fine mesh in space and in time. Therefore, simplex space-time elements will be used in the future. This method can also be helpful to capture the crystallization effects since the crystals grow much quicker near the flow interface, where the temperature is adequate.

Acknowledgements The authors gratefully acknowledge the support of the German Research Foundation (DFG) under program SFB 1120 “Precision Melt Engineering” - 236616214. The computations were conducted on computing clusters provided by the RWTH Aachen University IT Center and by the Jülich Aachen Research Alliance (JARA). Open access funding enabled and organized by Projekt DEAL.

References

[1] S. Elgeti and H. Sauerland, Arch. Comput. Methods Eng. **23**, 323–361 (2015).
[2] M. L. Williams, R. F. Landel, and J. D. Ferry, J. Am. Chem. Soc. **77**(14), 3701–3707 (1955).
[3] R. Malhotra and J. Dymond, Int. J. Thermophys. **633**, 941–951 (1988).
[4] Z. Yang, H. Peng, W. Wang, and T. Liu, J. Appl. Polym. Sci. **116**, 2658–2667 (2010).
[5] K. Nakamura, K. Katayama, and T. Amano, J. Appl. Polym. Sci. **17**, 1031–1041 (1973).
[6] J. D. Hoffman and R. L. Miller, Polymer **38**, 1031–1041 (1997).
[7] J. Donea and A. Huerta, Finite element methods for flow problems (John Wiley & Sons, New York City, 2003).
[8] M. Behr, Int. J. Numer. Meth. Fluids **57**, 1421-1434 (2008).
[9] V. Karyofylli, M. Frings, S. Elgeti, and M. Behr, Int. J. Numer. Meth. Fluids **86**, 218-230 (2018).
[10] J. Wang, C. Hopmann, M. Röbig, T. Hohlweck, C. Kahve, and J. Alms Polymers **12**, 409 (2020).
[11] R. Spina, M. Spekowius, and C. Hopmann, Mater. Des. **95**, 455–469 (2016).
[12] S. Mueller, E. Llewellin, and H. Mader, Proc. R. Soc. A **466**, 1201–1228 (2010).
[13] J. Alms, C. Hopmann, J. Wang, and T. Hohlweck, Polymers **12**, 1515 (2020).
[14] Y. Mubarak, E. Harkin-Jones, P. Martin, and M. Ahmad, Polymer **42**, 3171–3182 (2001).
[15] B. Wunderlich, Macromolecular physics V2 (Elsevier, 2012).
[16] M. Speckowius, dissertation, RWTH Aachen University (2017).
[17] H. G. Elias, Makromoleküle: Chemische Struktur und Synthesen-Sechste (John Wiley & Sons, 2009).
[18] T. Chan and A. Isayev, Polym. Eng. Sci. **34**, 461–471 (1994).
[19] J. I. Lauritzen Jr and J. D. Hoffman, J. Res. Natl. Bur. Stand. **64**, 73 (1960).
[20] J. Guo and K. A. Narh, Adv. Polym. Technol. **21**, 214-222 (2002).
[21] V. Karyofylli, L. Wendling, M. Make, N. Hosters, and M. Behr, Comput. Fluids **192** (2019).